Journal of Natural Gas Science and Engineering 32 (2016) 423–438

Contents lists available at ScienceDirect

Journal of Natural Gas Science and Engineering

journal homepage: www.elsevier.com/locate/jngse

Numerical study of a stress dependent triple porosity model for shale gas reservoirs accommodating gas diffusion in kerogen

Guijie Sang [a, b, *], Derek Elsworth [b], Xiexing Miao [a], Xianbiao Mao [a], Jiehao Wang [a, b]

[a] State Key Laboratory for Geomechanics & Deep Underground Engineering, China University of Mining & Technology, Xuzhou, Jiangsu, 221116, China
[b] John and Willie Leone Family Department of Energy and Mineral Engineering, EMS Energy Institute and G3 Center, Pennsylvania State University, University Park, PA 16802, USA

ARTICLE INFO

Article history:
Received 18 January 2016
Received in revised form
23 March 2016
Accepted 15 April 2016
Available online 20 April 2016

Keywords:
Shale-gas interaction
Triple porosity
Effective stress
Permeability evolution
Transport
Gas production

ABSTRACT

A model accommodating multi-scale pores containing kerogen within an inorganic matrix is used to explore the complex multi-mechanistic transport mechanisms of shale gas reservoirs. These include the complex evolution of pressure, diffusion and flow within both kerogen and inorganic components and their interaction with effective stresses. A general poromechanical model is proposed considering desorption and molecular diffusion in the kerogen, viscous flow in the inorganic matrix and fracture system, and composite deformation of the triple porosity assemblage. The model is verified by history matching against field data for gas production rate. The simulation results indicate that the pattern of gas flow is sequential during gas depletion – pressure first declines in the fracture, followed by the inorganic phase and then in the kerogen. The evolution of permeability is pressure dependent and the evolution of pressure is closely related to the intrinsic gas diffusion coefficient in the kerogen, inorganic matrix intrinsic permeability and fracture intrinsic permeability. A series of sensitivity analyses are completed to define key parameters affecting gas production. The study shows that dominant influence of the fracture network in acting as the main permeable conduit. The intrinsic permeability and porosity of the fracture have a positive correlation with gas production, while fracture spacing has a negative correlation to gas production. Kerogen also plays a critical role in gas production for shale reservoirs with higher total organic carbon. The enhancement of inorganic matrix permeability and gas diffusion coefficient in kerogen could efficiently guarantee a long-term gas production with a higher rate.

1. Introduction

Unconventional gas resources such as shale gas and coalbed methane show significant potential to offset declining conventional natural gas production. Modeling is an important way to reveal gas storage and transport mechanisms in such unconventional reservoirs.

Previous single/dual porosity models (Seidle et al., 1995; Palmer et al., 1996; Shi and Durucan, 2004; Zhang et al., 2008) are either pressure-dependent or strain-dependent, which contribute to reveal how the effective stress and adsorption-induced shrinkage influence coal seam permeability. In these cases, however, the effective stress, is based on the effective stress law for single porosity media, which may not be applicable for shale gas reservoirs since the transport mechanisms may differ between porous matrix and fracture network. Such models may be substituted for more complex models that accommodate the impact of the dual porosity medium on system compliance (Wu et al., 2010). Such models include the roles of deformation for single gas phase (Wu et al., 2010) to describe the evolution of porosity and permeability in the coalbed matrix and fracture system respectively under situ ground stress. In this, the gas flow obeys Darcy's law and the model is applicable to the full range of mechanical boundary conditions, from invariant total stress to restrained displacement. Similar models are available to accommodate nonlinear permeability models (Wu et al., 2011) including P-M models that accommodate gas diffusion and significant impact of Klinkenberg effects (Liu et al., 2015). These dual porosity models (Wu et al., 2010, 2011; Liu et al., 2015) are based on the law of effective stress for dual porosity media (Elsworth and Bai, 1992). However, these still

* Corresponding author. State Key Laboratory for Geomechanics & Deep Underground Engineering, China University of Mining & Technology, Xuzhou, Jiangsu, 221116, China.
E-mail address: gjsang@yahoo.com (G. Sang).

http://dx.doi.org/10.1016/j.jngse.2016.04.044
1875-5100/

may not be applicable to describe the complex gas flow and transport mechanisms in shale gas reservoirs due to the different sorption behavior and flow regimes between kerogen pockets and the inorganic solid medium (Yan et al., 2013a). Furthermore, some triple porosity models (Al-Ahmadi et al., 2011; Dehghanpour et al., 2011; Tivayanonda et al., 2012) consider macro fractures, micro fractures and matrix as a triple porosity medium, with gas flowing from matrix to micro fracture, and then to the macro fractures. Such models take no consideration of molecular diffusion within nanopores within the matrix. Some other triple porosity models are available to accommodate gas diffusion in kerogen within matrix and gas flow through matrix nanopores to fractures (Huang et al., 2015) including the model that accommodates the significance of dividing matrix into kerogen and inorganic matrix (Zhang et al., 2015). The model (Huang et al., 2015) might not be applicable due to the assumption that methane molecules could also be adsorbed on surfaces of inorganic materials.

The existence of nanopores in shale reservoirs has been verified by ultra-high pressure mercury injection (Katsube, 2000; Javadpour et al., 2007), back-scattered scanning electron microscopy (SEM) (Loucks et al., 2009) and atomic force microscopy AFM (Javadpour, 2009). The 2D focused-ion-beam SEM image (Kang et al., 2011; Ambrose et al., 2012; Akkutlu et al., 2012) of Fig. 1(a) shows that the organic matter contains finely dispersed porous kerogen pockets imbedded within inorganic materials (minerals/clay/silica), mainly including the organic micropores (<2 nm) and mesopores (2–50 nm). Pore sizes less than 100 nm are nearly exclusively found in the kerogen matrix, while the majority of pores in the inorganic matrix and fractures have much larger dimensions (Wasaki et al., 2014). Since the flow regime is sensitive to pore sizes (Ziarani and Aguilera, 2012) and their distribution, different types of fluid flow regimes should be conditioned according to the multi-scale pore sizes in shale gas reservoirs as is shown in Fig. 1(b).

In addition, the organic nanopores in kerogen have a relatively large internal surface area covered by a monolayer of methane molecules (approximately 2.8 $\times$ 10^{24} nm^3 for one ton of shale) despite the small dimension of the nanopores (Kang et al., 2011). Thus, the porous kerogen pockets are ideal sites for the storage of shale gas in the adsorbed phase due to the strong affinity (Van de Vaals forces) between hydrocarbon molecules and organic materials associated with the nanopore surface. Conversely, the amount of shale gas adsorbed in the inorganic pores is negligible due to the week affinity between hydrocarbon fluids and inorganic materials. Correspondingly, the relatively larger pores in the inorganic matrix contain a dominantly higher percentage of free gas compared to adsorbed gas (Wasaki et al., 2014).

The different types of gas flow and storage behaviors in the kerogen and the inorganic matrix prompt the conceptual triple porosity model shown in Fig. 2. This accommodates the three different media and their different characteristics, *viz*: the porous kerogen matrix (organic material), the porous inorganic matrix (inorganic material) and the fractured solid system (including both naturally fractured solid media and hydraulically fractured solid media). For the triple porosity model, the composite deformation of the triple porosity assemblage is coupled with gas transport in the three different systems to accommodate desorption and molecular diffusion in the kerogen, and viscous flow in the inorganic matrix and fracture system.

2. Triple porosity model for fractured porous shale

We develop a triple porosity that accommodates transport from a kerogen pocket into pores within an inorganic matrix, and from here into fractures. The mechanical and transport constitutive models are developed for this triple porosity system and combined into conservation equations for momentum and mass to define the field equations.

2.1. Assumptions

There are several assumptions applied to this triple porosity model.

(a) The shale reservoir is a fractured porous medium containing kerogen, inorganic matter and fractures. Each medium is isotropic, homogeneous and linear elastic.
(b) All strains is infinitesimal and the system is isothermal. Gas sorption follows Langmuir isothermal behavior.
(c) A single gas phase is (methane) is considered with assumed constant viscosity.
(d) Gas adsorption occurs only in the kerogen pockets, i.e., the kerogen contains gas in both free phase and adsorbed phase,

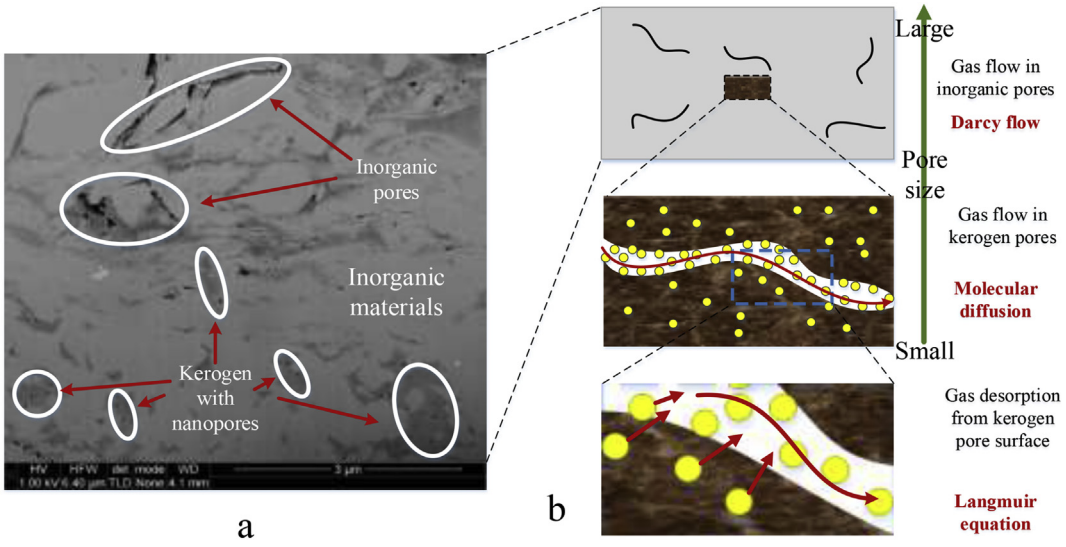

Fig. 1. (a) 2D FIB/SEM image of shale showing finely dispersed kerogen pockets imbedded in inorganic clays (Ambrose et al., 2012). (b) Schematic of gas desorption and flow pattern in kerogen and inorganic pores (modified from Javadpour et al. (2007), Song (2010)).

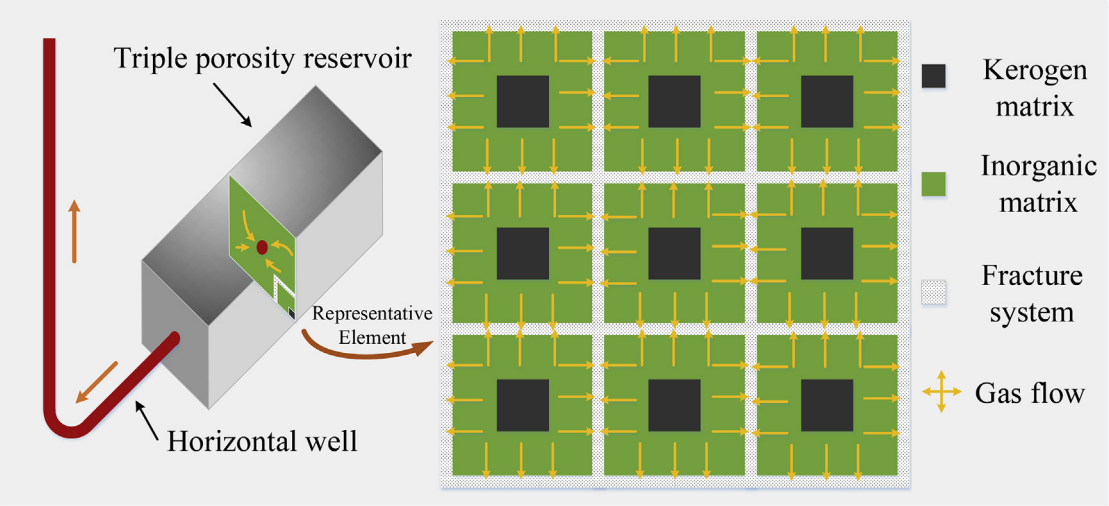

Fig. 2. Conceptual triple porosity model of shale gas reservoir.

while gas in the inorganic matrix and the fracture system occurs merely in the free phase.

2.2. Deformation of fractured porous shale

The equilibrium equation for a fractured porous medium can be expressed as

$$\sigma_{ij,j} + f_i = 0 \tag{1}$$

where σ_{ij} denotes the total stress tensor of a fractured porous shale element, and f_i is the body force. The following uses the normal Einstein notation: a comma followed by subscripts denotes differentiation with respect to spatial coordinates and repeated indices in the same monomial imply summation over the range of the indices (generally1–3, unless otherwise indicated) (Detournay and Cheng, 1993).

According to the effective stress law for multi-porous media (Elsworth and Bai, 1992; Mian et al., 1999), the effective stress for the fractured porous shale can be expressed as

$$\sigma'_{ij} = \sigma_{ij} - \left(\alpha p_1 + \beta p_2 + \gamma p_f\right)\delta_{ij} \tag{2}$$

where δ_{ij} is the Kronecker delta which is 1 when $i = j$ and 0 for all other cases. p_1 is the pore pressure in the kerogen matrix, p_2 is pore pressure in the inorganic matrix, and p_f is the gas pressure in the fracture system. In this paper, we adopt a sign convention of compressive stress as positive, with subscripted 1 representing the kerogen, 2 the inorganic system and f the fracture system. α, β and γ are effective stress coefficients for fractured porous media expressed as (Mian et al., 1999)

$$\begin{cases} \alpha = 1 - \dfrac{K}{K_1} \\ \beta = 1 - \dfrac{K}{K_2} \\ \gamma = 1 - \dfrac{K}{K_f} \end{cases} \tag{3}$$

where K_1 is the bulk modulus of the porous kerogen, K_2 the bulk modulus of the porous inorganic matrix, and K_f the modified fracture stiffness (Wu et al., 2010). K is the modified bulk modulus of the fractured porous shale, defined by the elastic properties of the triple media. The expressions for these parameters are defined as,

$$\begin{cases} C_1 = \dfrac{1}{E_1},\ C_2 = \dfrac{1}{E_2},\ C_3 = \dfrac{1}{K_f},\ D = \dfrac{1}{C_1 + C_2 + C_3} \\ K = \dfrac{D}{3(1-2\nu)},\ G = \dfrac{D}{2(1+\nu)} \end{cases} \tag{4}$$

where G and ν are the shear modulus and the Poisson ratio of fractured porous shale, respectively.

Considering adsorption, the constitutive relation for the linear elastic deformed shale becomes

$$\sigma'_{ij} = G(u_{i,j} + u_{j,i}) + \lambda u_{k,k}\delta_{ij} - K\varepsilon_s\delta_{ij} \tag{5}$$

where $\lambda = K - 2G/3$ is the Lame constant and u is the displacement of the fractured porous shale. Sorption-induced strain ε_s is given by the Langmuir isotherm (Langmuir, 1918) for gas adsorption and desorption process in the kerogen matrix system as

$$\varepsilon_s = \frac{\varepsilon_L p_1}{p_L + p_1} \tag{6}$$

where ε_L is the Langmuir volumetric strain, a constant at infinite pore pressure. The Langmuir constant P_L represents the pore pressure at which the measured volumetric strain is equal to $0.5\varepsilon_L$.

Solving Eqs. (1), (2), (5) and (6) yields the Navier-type equation as

$$Gu_{i,jj} + \frac{G}{1-2\nu}u_{k,kj} = -\alpha p_{1,i} - \beta p_{2,i} - \gamma p_{f,i} + K\varepsilon_{s,i} - f_i \tag{7}$$

Taking the three types of media (fractured solid media, porous inorganic matrix and porous kerogen matrix) into consideration, separately, there exist three skeletal stresses that control the deformation of each media. The skeletal stresses are shown in Fig. 3. For the nested form of the media, with fractures encapsulating inorganic matrix that in turn encapsulates the kerogen, the skeletal stresses can be expressed as

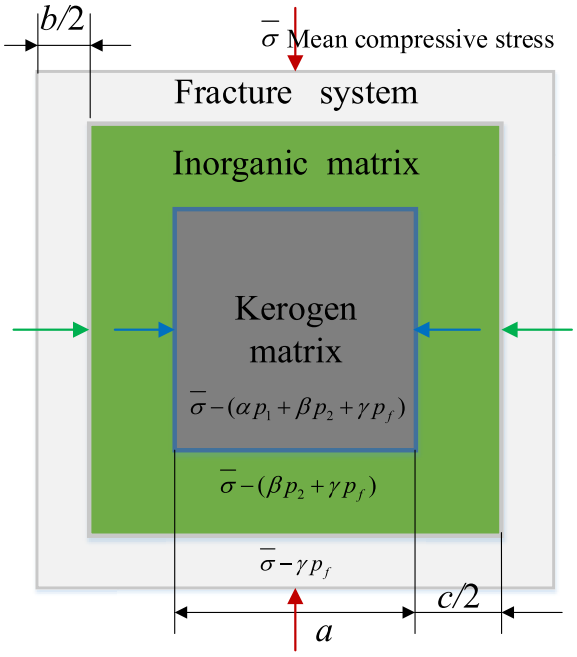

Fig. 3. Schematic of skeletal stresses within a representative element volume (REV) for the triple porosity model.

$$\begin{cases} \sigma_{ij}^{e1} = \sigma_{ij} - \left(\alpha p_1 + \beta p_2 + \gamma p_f\right)\delta_{ij} \\ \sigma_{ij}^{e2} = \sigma_{ij} - \left(\beta p_2 + \gamma p_f\right)\delta_{ij} \\ \sigma_{ij}^{ef} = \sigma_{ij} - \gamma p_f \delta_{ij} \end{cases} \tag{8}$$

Considering the kerogen matrix, inorganic matrix and fractured solid system as separate linearly elastic media, the constitutive equation for each medium can be generally expressed as

$$\varepsilon_{ij} = \frac{1}{2G'}\sigma_{ij}^{em} - \left(\frac{1}{6G'} - \frac{1}{9K'}\right)\sigma_{kk}^{em}\delta_{ij} + \frac{\varepsilon_s}{3}\delta_{ij} \tag{9}$$

where the sorption-induced volumetric strain $\varepsilon_s = 0$ for the inorganic matrix and fractured solid system, but cannot be neglected for the kerogen matrix where $\varepsilon_s \neq 0$. G' denotes G_1 for the kerogen matrix, G_2 for the inorganic matrix, and G_f for the fractured solid system; K' denotes K_1 for the kerogen matrix, K_2 for the inorganic matrix, and K_f for the fractured solid system. m denotes 1 for kerogen, 2 for the inorganic fraction and f for the fractured solid system.

For compression positive, the mean compressive stress is $\bar{\sigma} = \sigma_{kk}/3 = (\sigma_{11} + \sigma_{22} + \sigma_{33})/3$ and the volumetric strain is $\varepsilon_v = \varepsilon_{kk} = \varepsilon_{11} + \varepsilon_{22} + \varepsilon_{33}$. Substituting the skeletal stresses of Eq. (8) into the constitutive relation of Eq. (9) yields,

$$\begin{cases} \varepsilon_{v1} = \frac{1}{K_1}\left[\bar{\sigma} - \left(\alpha p_1 + \beta p_2 + \gamma p_f\right)\right] + \varepsilon_s \\ \varepsilon_{v2} = \frac{1}{K_2}\left[\bar{\sigma} - \left(\gamma p_f + \beta p_2\right)\right] \\ \varepsilon_{vf} = \frac{1}{K_f}\left(\bar{\sigma} - \gamma p_f\right) \end{cases} \tag{10}$$

For an isotropic medium, the total linear strain for the shale REV can be expressed as

$$\varepsilon_l = \frac{\Delta a + \Delta c + \Delta b}{a+b+c} = \frac{a\cdot\frac{1}{3}\varepsilon_{v1} + c\cdot\frac{1}{3}\varepsilon_{v2} + b\cdot\frac{1}{3}\varepsilon_{vf}}{a+b+c} \tag{11}$$

where a, c and b are the width of the kerogen block, inorganic block and fracture system respectively, shown in Fig. 3. b represents the equivalent fracture aperture with fracture spacing defined as $s = a + c$.

The total volumetric strain for a REV is $\varepsilon_v = 3\varepsilon_l$. Combining Eq. (10) with (11) yields

$$\bar{\sigma} = \frac{a+b+c}{N_1}\varepsilon_v + \frac{\alpha}{N_1}\frac{a}{K_1}p_1 + \left(1 - \frac{b}{N_1 K_f}\right)\beta p_2 + \gamma p_f - \frac{a}{N_1}\varepsilon_s \tag{12}$$

where N_1 is defined by the elastic properties of the shale reservoir and the size of REV as

$$N_1 = \frac{a}{K_1} + \frac{c}{K_2} + \frac{b}{K_f} \tag{13}$$

From Eq. (12), it is clear that the average total stress $\bar{\sigma}$ is controlled by the total volumetric strain of the REV ε_v, the sorption-induced volumetric strain ε_s and pore pressure in kerogen, inorganic matrix system and fractured solid system p_1, p_2 p_f.

2.3. Triple porosity model for fractured porous shale

2.3.1. Dynamic porosity and permeability model for the porous inorganic matrix system

The evolution of porosity for the inorganic matrix system may be described as (see "Appendix")

$$\Phi_2 = \frac{1}{1+S_2}\left[(1+S_{20})\Phi_{20} + (\beta+\gamma)(S_2 - S_{20})\right] \tag{14}$$

where,

$$\begin{cases} S_2 = \frac{1}{K_2 N_1}\left[(a+b+c)\varepsilon_v + \frac{a}{K_1}\alpha p_1 + \left(N_1 - \frac{b}{K_f} - \frac{N_1}{\beta}\right)\beta p_2 + N_1(\gamma-1)p_f - a\varepsilon_s\right] \\ S_{20} = \frac{1}{K_2 N_1}\left[\frac{a}{K_1}\alpha p_{10} + \left(N_1 - \frac{b}{K_f} - \frac{N_1}{\beta}\right)\beta p_{20} + N_1(\gamma-1)p_{f0} - a\varepsilon_{s0}\right] \\ \varepsilon_{s0} = \frac{\varepsilon_L p_{10}}{p_L + p_{10}} \end{cases} \tag{15}$$

where Φ_{20} is the intrinsic porosity of the inorganic matrix at p_{10}, p_{20} and p_{f0}, which are the initial pressure in the kerogen matrix system, inorganic matrix system and fracture system, respectively. ε_{s0} is the

initial sorption-induced strain. The initial volumetric strain is zero. Other parameters are as described previously.

The cubic relationship between porosity and permeability of the porous medium is given by Chilingar (1964)

$$\frac{k_2}{k_{20}} = \left(\frac{\Phi_2}{\Phi_{20}}\right)^3 \tag{16}$$

Substituting Eq. (14) into (16) yields the permeability model for the inorganic matrix system as

$$\frac{k_2}{k_{20}} = \left[\frac{1+S_{20}}{1+S_2} + \frac{(\beta+\gamma)(S_2-S_{20})}{\Phi_{20}(1+S_2)}\right]^3 \tag{17}$$

2.3.2. Dynamic porosity model for porous kerogen system

According to Eq. (10), the volumetric strain is

$$\varepsilon_{v1} = \frac{\Delta V_1}{V_1} = \frac{1}{K_1}\left[\overline{\sigma} - \left(\alpha p_1 + \beta p_2 + \gamma p_f\right)\right] + \varepsilon_s \tag{18}$$

Using a similar analytical method for porosity evolution in the porous inorganic system (discussed in the Appendix), considering the sorption effect, the evolution of porosity in the kerogen matrix system is

$$\Phi_1 = \frac{1}{1+S_1}[(1+S_{10})\Phi_{10} + (\alpha+\beta+\gamma)(S_1-S_{10})] \tag{19}$$

where,

$$\begin{cases} S_1 = \dfrac{1}{K_1 N_1}\left[(a+b+c)\varepsilon_v + \left(\dfrac{\alpha a}{K_1} - N_1\right)p_1 + \left(N_1 - \dfrac{b}{K_f} - \dfrac{N_1}{\beta}\right)\beta p_2 + N_1(\gamma-1)p_f - a\varepsilon_s\right] \\ S_{10} = \dfrac{1}{K_1 N_1}\left[\left(\dfrac{\alpha a}{K_1} - N_1\right)p_{10} + \left(N_1 - \dfrac{b}{K_f} - \dfrac{N_1}{\beta}\right)\beta p_{20} + N_1(\gamma-1)p_{f0} - a\varepsilon_{s0}\right] \end{cases} \tag{20}$$

where Φ_{10} is the intrinsic porosity of the kerogen matrix at p_{10}, p_{20} and p_{f0}. The initial volumetric strain is zero. Other parameters are as described previously.

2.3.3. Dynamic porosity and permeability model for fracture system

For the fracture system, the porosity can be defined as a function of the fracture spacing s and the fracture aperture b as $\Phi_f = 3b/s$, while the permeability can be defined as $k_f = b^3/12s$ (Liu et al., 1999; Robertson et al., 2006). The change in porosity and permeability can then be described as

$$\begin{cases} d\Phi_f = \dfrac{3b}{s}\left(\dfrac{db}{b} - \dfrac{ds}{s}\right) = \Phi_f\left(\dfrac{db}{b} - \dfrac{ds}{s}\right) \cong \Phi_f\left(\dfrac{d\varepsilon_{vf}}{3} - \dfrac{d\varepsilon_{vm}}{3}\right) \\ dk_f = k_f\left(\dfrac{3db}{b} - \dfrac{ds}{s}\right) = k_f\left(d\varepsilon_{vf} - \dfrac{1}{3}d\varepsilon_{vm}\right) \end{cases} \tag{21}$$

where ε_{vm} is expressed by volumetric strain of the inorganic matrix system ε_{v2} and the kerogen matrix system ε_{v1} as

$$\varepsilon_{vm} = \frac{3\Delta s}{s} = \frac{3(\Delta a + \Delta c)}{a+c} = \frac{3\left(a\frac{1}{3}\varepsilon_{v1} + c\frac{1}{3}\varepsilon_{v2}\right)}{a+c} = \frac{a\varepsilon_{v1} + c\varepsilon_{v2}}{a+c} \tag{22}$$

Considering the initial volumetric strain to be zero, integrating Eq. (21) yields

$$\begin{cases} \dfrac{\Phi_f}{\Phi_{f0}} = e^{\frac{1}{3}(\varepsilon_{vf} - \varepsilon_{vm})} \cong 1 + \dfrac{1}{3}\left(\varepsilon_{vf} - \varepsilon_{vm}\right) \\ \dfrac{k_f}{k_{f0}} = e^{\varepsilon_{vf} - \frac{1}{3}\varepsilon_{vm}} \cong 1 + \left(\varepsilon_{vf} - \dfrac{1}{3}\varepsilon_{vm}\right) \end{cases} \tag{23}$$

Solving Eqs. (10), (12), (22) and (23) yields the dynamic porosity and permeability for the fracture system as

$$\begin{cases} \Phi_f = \Phi_{f0} + \dfrac{\Phi_{f0}}{3}\left\{\dfrac{(a+b+c)N_2}{N_1}\varepsilon_v + \left(\dfrac{N_2}{N_1} + \dfrac{1}{a+c}\right)\left[\dfrac{a}{K_1}\alpha p_1 + \left(\dfrac{a}{K_1} + \dfrac{c}{K_2}\right)\beta p_2\right] - \dfrac{a}{a+c}\varepsilon_s\right\} \\ k_f = k_{f0} + \dfrac{1}{3}k_{f0}\left\{\dfrac{(a+b+c)N_3}{N_1}\varepsilon_v + \left(\dfrac{N_3}{N_1} + \dfrac{1}{a+c}\right)\left[\dfrac{a}{K_1}\alpha p_1 + \left(\dfrac{a}{K_1} + \dfrac{c}{K_2}\right)\beta p_2\right] - \dfrac{a}{a+c}\varepsilon_s\right\} \end{cases} \tag{24}$$

where Φ_{f0} and k_{f0} are the fracture intrinsic porosity and the fracture intrinsic permeability. N_2 and N_3 are defined by the elastic properties of the shale reservoir and the size of the REV as

$$\begin{cases} N_2 = \dfrac{1}{K_f} - \dfrac{a}{(a+c)K_1} - \dfrac{c}{(a+c)K_2} \\ N_3 = N_2 + \dfrac{2}{K_f} = \dfrac{3}{K_f} - \dfrac{a}{(a+c)K_1} - \dfrac{c}{(a+c)K_2} \end{cases} \tag{25}$$

2.4. Governing equation for gas flow and transport in triple porosity shale reservoir

2.4.1. Diffusion of adsorbed gas in kerogen system

According to the isothermal Langmuir relation, gas desorbs from the kerogen surface to the pore space and is then carried by the pressure drop. As desorption continues, the gas concentration gradient between the bulk kerogen and the surface of the kerogen pocket drives gas diffusion in the solid kerogen. According to Fick's law and mass conservation,

$$\frac{\partial m_1}{\partial t} + \nabla(-D\nabla m_1) = -Q_{1-2} \tag{26}$$

where D is the molecular diffusion coefficient in the porous kerogen, m^2/s. Q_{1-2}, $kg/(m^3\ s)$, is the gas exchange rate from the kerogen to the inorganic system due to diffusion (obeying Fick's law rather than Darcy's law); t is elapsed time, s; and the gas mass content m_1, kg/m^3, is the quantity of both free gas and adsorbed gas per volume of the kerogen matrix system, expressed by

$$m_1 = \rho_{g1}\Phi_1 + \rho_{ga}\rho_s\frac{V_L p_1}{p_1 + p_L} \tag{27}$$

The gas exchange rate Q_{1-2} for diffusion from the kerogen matrix to the inorganic matrix can be expressed as (Mora et al., 2009; Wang et al., 2012a)

$$Q_{1-2} = \frac{1}{\tau'}\left(\rho_{g1} - \rho_{g2}\right) \tag{28}$$

where ρ_{g1} and ρ_{g2} are the gas density in the kerogen and the inorganic system, respectively, given by the state equation of an ideal gas; τ' is the diffusive time, s, generally expressed as

$$\tau' = \frac{1}{\sigma_1 D} \tag{29}$$

The shape factor σ_1, m^{-2}, is defined as (Lim and Aziz, 1995)

$$\sigma_1 = \frac{3\pi^2}{a^2} \tag{30}$$

where a is the kerogen block width in a REV.

Since the pore sizes in the kerogen are of the order of nanometers, Knudsen diffusion should be considered in the porous kerogen system. The flow in a long straight pore can be described by the Knudsen diffusion coefficient (Javadpour et al., 2007; Ziarani and Aguilera, 2012). For the porous medium containing open pores (porosity) and interconnected pores (tortuosity), the actual path is longer than the minimum straight path. Knudsen flow through porous kerogen can be modeled using a modified form as

$$D_k = \frac{\Phi_1}{\tau}\frac{d}{3}\sqrt{\frac{8RT}{\pi M_g}} \tag{31}$$

where d is the diameter of the nanopore. Φ_1 and τ are the porosity and the tortuosity of the kerogen matrix, and Φ_1/τ is the porosity-tortuosity factor.

From Eq. (31), the diffusion coefficient of CH_4 in kerogen can be deduced as

$$D_k = D_{k0}\frac{\Phi_1}{\Phi_{10}} \tag{32}$$

According to the state equation of an ideal gas

$$\rho_g = \frac{M_g}{RT}p \tag{33}$$

Combining Eqs. (26)–(33) yields the governing equation for gas flow in the kerogen system

$$\left[\Phi_1 + p_{ga}\rho_s\frac{V_L P_L}{(P_L+p_1)^2}\right]\frac{\partial p_1}{\partial t} + p_1\frac{\partial \Phi_1}{\partial t} + \nabla\left[-D_k\left(\Phi_1 + p_{ga}\rho_s\frac{V_L P_L}{(P_L+p_1)^2}\right)\nabla p_1\right] = -\omega_1(p_1 - p_2) \tag{34}$$

where ω_1, 1/s, is the transfer coefficient between the kerogen matrix and the inorganic matrix, also derived from Eqs. (26)–(33) (Lim and Aziz, 1995; Mora et al., 2009; Wang et al., 2012a).

$$\omega_1 = \frac{3\pi^2}{a^2}D_k \tag{35}$$

Substituting the partial derivative of Φ_1 with respect to time from Eq. (19) into Eq. (34), yields the final governing equation for gas diffusion with gas desorption in the kerogen as

$$\left[A + \frac{\alpha+\beta+\gamma-\Phi_1}{1+S_1}\frac{p_1}{K_1 N_1}\left(\frac{\alpha a}{K_1} - N_1 - \frac{a\varepsilon_L P_L}{(P_L+p_1)^2}\right)\right]\frac{\partial p_1}{\partial t} + \nabla[-D_k A\nabla p_1] = Q_1 \tag{36}$$

$$\begin{cases} A = \Phi_1 + p_{ga}\rho_s\dfrac{V_L P_L}{(P_L+p_1)^2} \\ Q_1 = -\omega_1(p_1 - p_2) - Q_{11}\dfrac{\partial \varepsilon_v}{\partial t} - Q_{12}\dfrac{\partial p_2}{\partial t} - Q_{13}\dfrac{\partial p_f}{\partial t} \\ Q_{11} = \dfrac{\alpha+\beta+\gamma-\Phi_1}{1+S_1}\dfrac{a+b+c}{N_1}\dfrac{p_1}{K_1} \\ Q_{12} = \dfrac{\alpha+\beta+\gamma-\Phi_1}{1+S_1}\left(\beta - \dfrac{\beta b}{N_1 K_f} - 1\right)\dfrac{p_1}{K_1} \\ Q_{13} = \dfrac{\alpha+\beta+\gamma-\Phi_1}{1+S_1}(\gamma - 1)\dfrac{p_1}{K_1} \end{cases} \tag{37}$$

2.4.2. Gas flow in the inorganic system and fracture system

These components host viscous flow, driven by pressure

gradient. Gas flow in the inorganic system and fracture network follows Darcy's law and the mass conservation law

$$\begin{cases} \dfrac{\partial m_2}{\partial t} + \nabla\left(\rho_{g2}\overrightarrow{q_{g2}}\right) = Q_{1-2} - Q_{2-f} \\ \dfrac{\partial m_f}{\partial t} + \nabla\left(\rho_{gf}\overrightarrow{q_{gf}}\right) = Q_{2-f} + Q_s \end{cases} \tag{38}$$

where ρ_g is the gas density, kg/m^3, given by the state equation of an ideal gas; $\boldsymbol{q}_{g2}$ and $\boldsymbol{q}_{gf}$ are the Darcy velocity vector in the inorganic system and fracture system respectively, m/s; Q_{2-f}, kg/(m^3 s), is the gas exchange rate from matrix to fracture due to the pressure gradient during gas production; Q_s, is the mass source due to external injection or extraction, kg/(m^3 s); t is elapsed time, s.

The mass of gas m contains only free-phase gas in the porous inorganic matrix system and in the fracture network.

$$m = \rho_g \Phi \tag{39}$$

where Φ is the porosity of the porous inorganic system or the fracture system.

The gas exchange rate Q_{2-f} for viscous flow from the inorganic matrix system to the fracture system can be described as (Warren et al., 1963; Lim and Aziz, 1995; Mora et al., 2009)

$$Q_{2-f} = \sigma_2 \frac{k_2}{\mu}\left(\rho_{g2} - \rho_{gf}\right) \tag{40}$$

where σ_2 is the shape factor for three sets of fractures determined by the fracture spacing s ($s = a + c$) as (Lim and Aziz, 1995)

$$\sigma_2 = \frac{3\pi^2}{(a+c)^2} \tag{41}$$

Ignoring gravity effects, the gas velocity vector in the inorganic system and the fracture network can be described by Darcy's law.

$$\overrightarrow{q_g} = -\frac{k}{\mu}\nabla p \tag{42}$$

Substituting Eqs. (39)–(42) into (38), the governing equation for gas flow in the inorganic system and the fracture system can be obtained as

$$\begin{cases} \Phi_2 \dfrac{\partial p_2}{\partial t} + p_2 \dfrac{\partial \Phi_2}{\partial t} + \nabla\left(-\dfrac{k_2}{\mu} p_2 \nabla p_2\right) = \omega_1(p_1 - p_2) - \omega_2\left(p_2 - p_f\right) \\ \Phi_f \dfrac{\partial p_f}{\partial t} + p_f \dfrac{\partial \Phi_f}{\partial t} + \nabla\left(-\dfrac{k_f}{\mu} p_f \nabla p_f\right) = \omega_2\left(p_2 - p_f\right) \end{cases} \tag{43}$$

where ω_2 is the transfer coefficient between inorganic matrix and fracture, which is also derived from Eqs. (38)–(42) (Warren et al., 1963; Lim and Aziz, 1995; Mora et al., 2009), expressed by

$$\omega_2 = \frac{3\pi^2}{(a+c)^2}\frac{k_2}{\mu} \tag{44}$$

Substituting the partial derivative of Φ_2 with respect to time from Eq. (14) into Eq. (43), results in the final gas flow equation in the inorganic matrix system as

$$\left[\Phi_2 + \frac{\beta + \gamma - \Phi_2}{1 + S_2}\frac{p_2}{K_2}\left(\beta - \frac{\beta b}{N_1 K_f} - 1\right)\right]\frac{\partial p_2}{\partial t} + \nabla\left(-\frac{k_2}{\mu} p_2 \nabla p_2\right) = Q_2 \tag{45}$$

$$\begin{cases} Q_2 = \omega_1(p_1 - p_2) - \omega_2\left(p_2 - p_f\right) - Q_{21}\dfrac{\partial \varepsilon_v}{\partial t} - Q_{22}\dfrac{\partial p_1}{\partial t} - Q_{23}\dfrac{\partial p_f}{\partial t} + Q_{24}\dfrac{\partial \varepsilon_s}{\partial t} \\ Q_{21} = \dfrac{\beta + \gamma - \Phi_2}{1 + S_2}\dfrac{a + b + c}{N_1}\dfrac{p_2}{K_2} \\ Q_{22} = \dfrac{\beta + \gamma - \Phi_2}{1 + S_2}\dfrac{\alpha}{N_1}\dfrac{a}{K_1}\dfrac{p_2}{K_2} \\ Q_{23} = \dfrac{\beta + \gamma - \Phi_2}{1 + S_2}(\gamma - 1)\dfrac{p_2}{K_2} \\ Q_{24} = \dfrac{\beta + \gamma - \Phi_2}{1 + S_2}\dfrac{a}{N_1}\dfrac{p_2}{K_2} \end{cases} \tag{46}$$

From Eq. (24), the partial derivative of Φ_f with respect to fracture pressure p_f is zero: $\partial\Phi_f/\partial p_f = 0$, thus the fracture pressure p_f has no direct contribution to porosity evolution in the fracture system. Thus, the final gas flow equation can be expressed as

$$\Phi_f \frac{\partial p_f}{\partial t} + \nabla\left(-\frac{k_f}{\mu} p_f \nabla p_f\right) = \omega_2\left(p_2 - p_f\right) - p_f \frac{\partial \Phi_f}{\partial t} \tag{47}$$

defining gas flow in the fracture system.

3. Model description and model validation against field data

The coupled governing equations shown in Fig. 4 are a set of non-linear partial differential equations (PDEs). These are solved by COMSOL Multiphysics (FE-based multiphysics modeling), using solid mechanics and PDE solution (non-linear diffusion and flow equations) modules. The poromechanical model is implemented into a fully coupled representation of composite deformation of the triple porosity assemblage and gas flow and transport in the kerogen, inorganic matrix and fracture system.

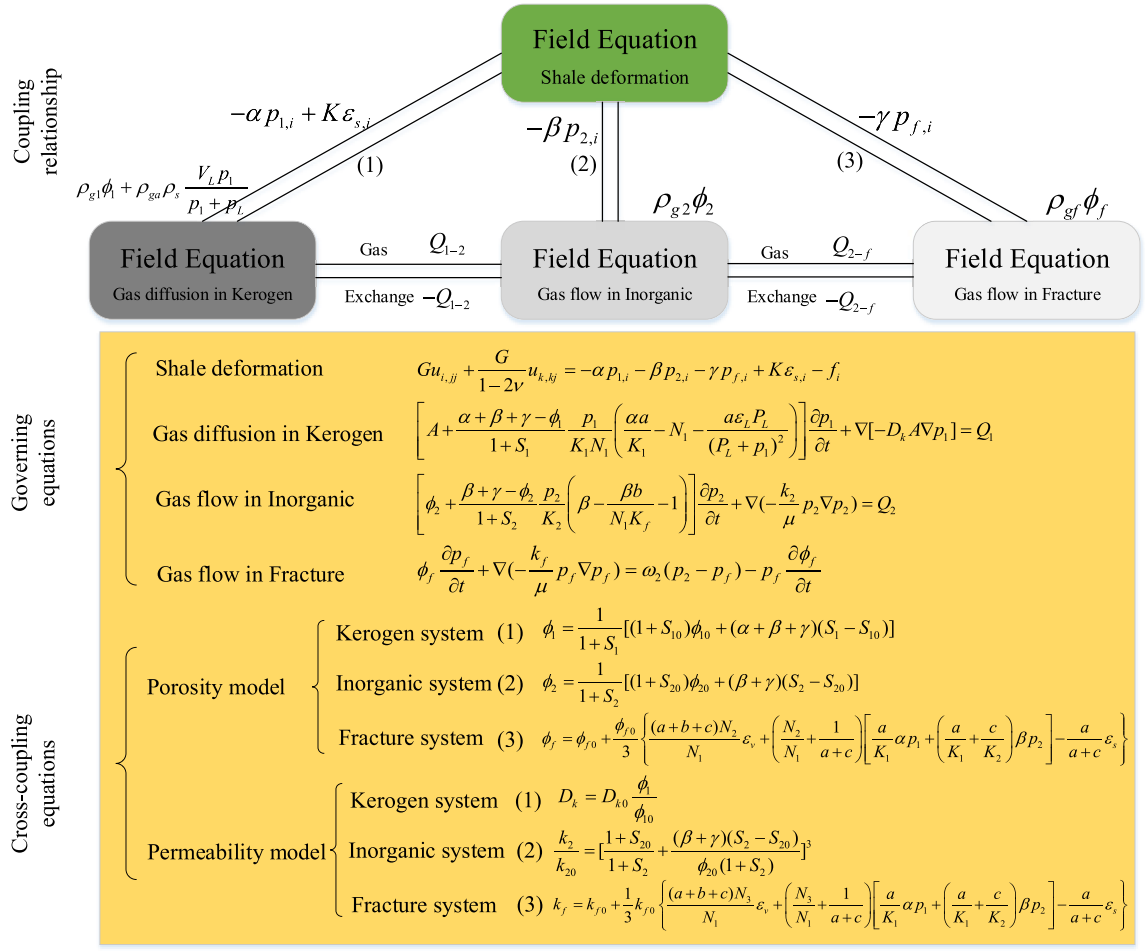

Fig. 4. Cross-coupling interactions between deformation, diffusion and flow for the triple porosity model.

3.1. Model description

The model of Fig. 5 is used to investigate the performance for this triple porosity model representing a shale gas reservoir. The production area is 400 × 400 m^2. The radius of the production well is 0.1 m. Due to the symmetry of the influence zone, only one quarter of the production area is simulated.

Boundary and initial conditions are required to solve the

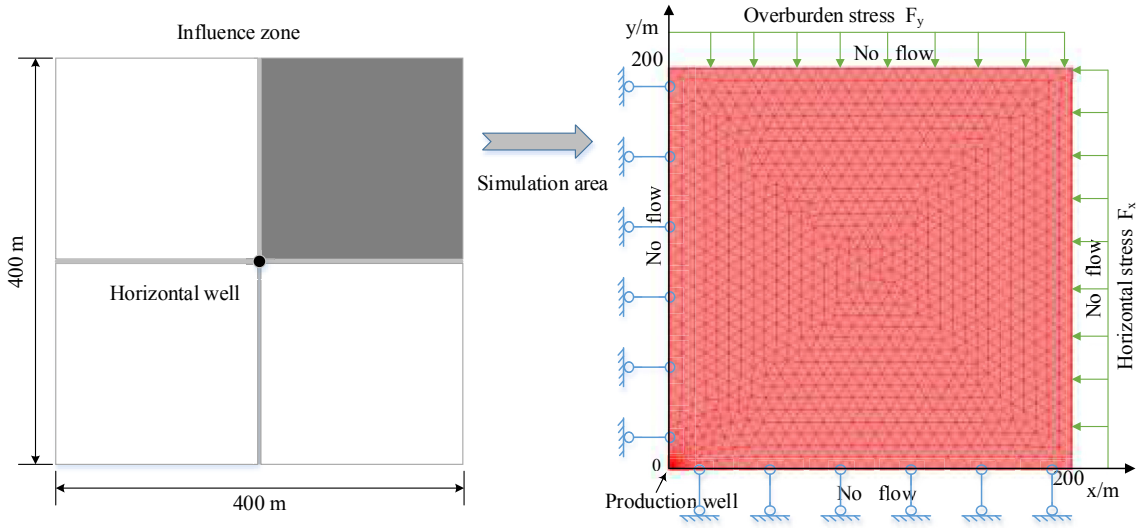

Fig. 5. Numerical model for gas production.

Table 1
Simulation parameters.

Parameters	Value	Unit
Young's modulus of shale E	32.75 (Goodway et al., 2006)	GPa
Poisson's ratio ν	0.2 (Aadnoy and Looyeh, 2011)	–
Bulk modulus of kerogen K_1	3.5–5 (Yan et al., 2013b)	GPa
Bulk modulus of inorganic matrix K_2	22	GPa
Modified fracture stiffness K_f	0.1 (Wu et al., 2010)	GPa
Depth h	1665	m
Horizontal well length L	904.6	m
Density of shale ρ	2580	kg/m^3
Langmuir pressure P_L	4.48	MPa
Langmuir volume V_L	2.72×10^{-3}	m^3/kg
Gas viscosity μ	2.01×10^{-5}	Pa·s
Langmuir volume strain of CH_4 ε_L	8.1×10^{-4} (Li and Elsworth, 2014)	–
Intrinsic porosity of kerogen matrix Φ_{10}	6	%
Diffusion coefficient of CH_4 in kerogen D_{k0}	1.0×10^{-20} (Etminan et al., 2014)	m^2/s
Intrinsic porosity of inorganic matrix Φ_{20}	6	%
Intrinsic permeability of inorganic matrix k_{20}	1.48×10^{-19} (1.5×10^{-4})	m^2 (md)
Initial reservoir pressure p_{init}	20.3	MPa
Well pressure p_w	3.45	MPa
Overburden stress gradient γ'	22.15 (Wang et al., 2013)	kPa/m
Reservoir temperature T	338.75	K
Universal gas constant R	8.314 (Zhang et al., 2015)	J/(K·mol)
Gas molecular weight M_g	16×10^{-3}	kg/mol

Table 2
Assumed values of parameters for the triple porosity model.

Parameters	Assumed value	Unit
Fracture intrinsic porosity Φ_{f0}	0.2	%
Fracture intrinsic permeability k_{f0}	3.25×10^{-17}	m^2
Kerogen matrix width a	1.0×10^{-4}	m
Inorganic matrix width c	0.15	m
Fracture aperture b	1.0×10^{-5}	m
Lateral stress ratio λ'	1.2	–

coupled interactions between deformation, diffusion and flow for the triple porosity model. Displacements are rollered on the left side and base. The top boundary is loaded by vertical crustal stress F_y, and the right boundary is loaded by horizontal crustal stress F_x. The vertical crustal stress F_y is the product of overburden stress gradient γ' and the depth of shale reservoir h. The ratio of the horizontal in-situ stress to vertical in-situ stress F_y/F_x is kept as λ' (For most cases, λ' ranges from 0.5 to 5). For gas flow, a constant well pressure p_w of 3.45 MPa is applied on the inner boundary of the production well and no-flow conditions are applied on all the other boundaries. The initial reservoir pressure in the numerical model is 20.3 MPa. The input parameters are listed in Tables 1 and 2, most of which are derived from the literature (Mengal, 2010; Al-Ahmadi et al., 2011).

To ensure the reliability and validity of the triple porosity model, validation is completed through history matching of field data. Gas production rate predictions between model and field data are explored for Barnett shale (Al-Ahmadi et al., 2011) as follows.

3.2. Model validation against field data

Field data of gas production rate for a horizontal well (Al-Ahmadi et al., 2011) with multistage hydraulic fracturing treatment producing at a constant well pressure are shown in Fig. 6. The gas production rate follows Wattenbarger Linear Flow Type-Curves (Wattenbarger et al., 1998). The gas production rate exhibits a slope of one-half on a log-log plot of rate vs time. This indicates a transient linear flow followed by boundary dominant flow (BDF). The early deviation from the trend indicates the possibility of skin effect due to the presence of water blocking gas flow to the well (Bello et al., 2010; Al Ahmadi et al., 2010) at early time.

History matching of field data from the Barnett shale is presented in Fig. 7. The model result shows a remarkable match with the field data. During the gas production process, free gas in the fracture network is the dominant component in early stage

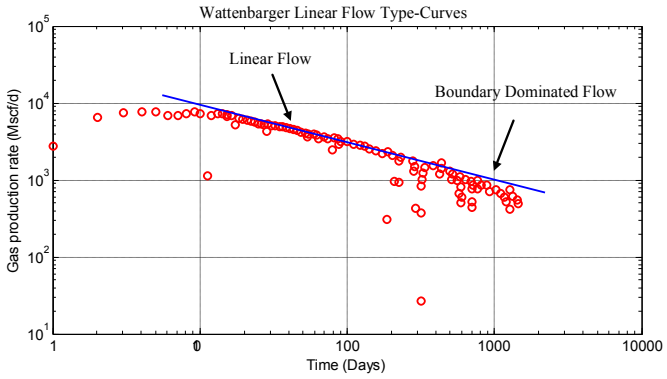

Fig. 6. Log-log plot of gas production rate vs. time for a horizontal well (modified from Al-Ahmadi et al. (2011)). The well exhibits long periods of transient linear flow, followed by BDF. The blue line indicates a slope of one-half. (For interpretation of the references to colour in this figure legend, the reader is referred to the web version of this article.)

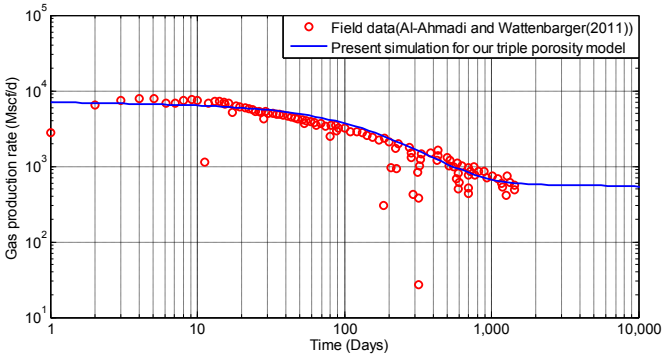

Fig. 7. Log-log plot of gas production rate vs. time for history matching.

production driven by the pressure gradient; the adsorbed phase is produced at later time when it desorbs from the kerogen, supplying the production well continuously. The gas production rate in the numerical simulation is slightly lower than the field data in the early stage. This might result from the fact that the hydraulic fracture and natural fractures in the model are a composite fractured solid system, leading to the underestimate of the intrinsic permeability of the fracture. Another small difference apparent in Fig. 7 is that the production rate at later time in the model holds near constant, while the field production data continue to drop. This may be because that, during simulation, the cumulative free gas from the fracture network and inorganic matrix system quickly depletes as production continues, while gas storage in the kerogen continues the long-term production. Other reasons for the later deviation may be due to BDF or the reduction of the drainage area of the well due to drilling of the nearby well (Al-Ahmadi et al., 2011). From this analysis, therefore, the proposed triple porosity model is applicable to the simulation of gas production.

4. Results and discussion

4.1. Pressure evolution

To better understand the gas flow sequence and gas transport mechanism in shale reservoirs during the gas depletion process, the pressure evolution in the kerogen matrix, inorganic matrix and fracture system at the position (100 m, 100 m) ~140 m away from the production well is conducted in this section.

Fig. 8 shows pressure evolution for the case of $D_{k0} = 1.0 \times 10^{-20}$ m^2/s, $k_{20} = 1.5 \times 10^{-3}$ md and $k_{f0} = 3.25 \times 10^{-17}$ m^2. Pressures within the different components decline at different rates. The fracture network has a much higher permeability so its pressure declines most rapidly. The initial pressures in kerogen pores, inorganic pores and fracture are equal. Due to the pressure gradient between the initial fracture pressure and the production well pressure, free gas stored in the fracture network begins to flow to the production well, causing pressure drawdown in the fracture network. Subsequently, the pressure

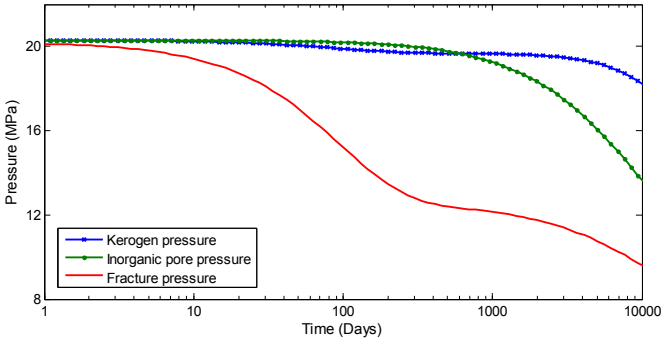

Fig. 8. Pressure evolution for the case of $D_{k0} = 1.0 \times 10^{-20}$ m^2/s, $k_{20} = 1.5 \times 10^{-3}$ md and $k_{f0} = 3.25 \times 10^{-17}$ m^2.

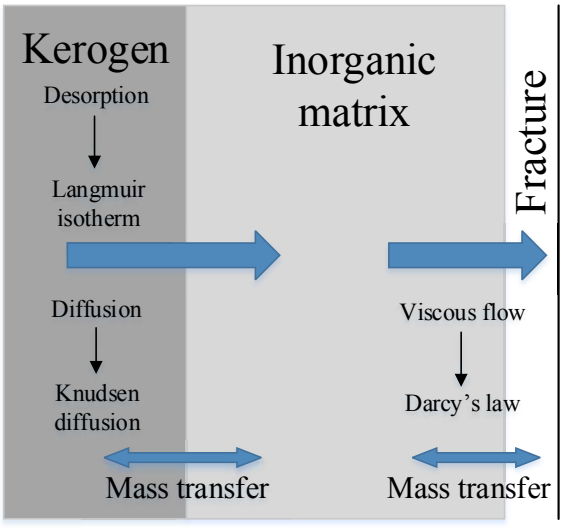

Fig. 9. Gas flow and transport sequence for series flow.

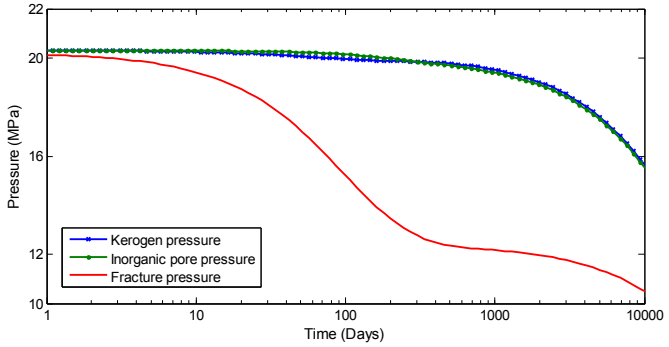

Fig. 10. Pressure evolution for the case of $D_{k0} = 1 \times 10^{-18}$ m^2/s, $k_{20} = 1.5 \times 10^{-3}$ md and $k_{f0} = 3.25 \times 10^{-17}$ m^2.

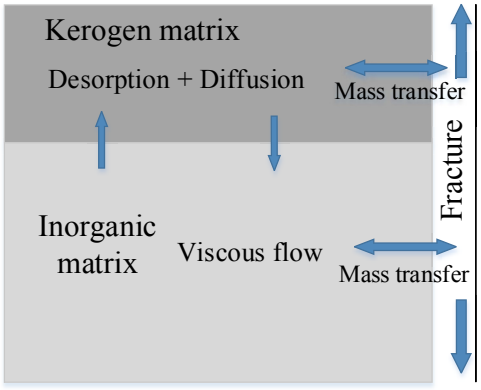

Fig. 11. Gas flow and transport sequence for parallel flow.

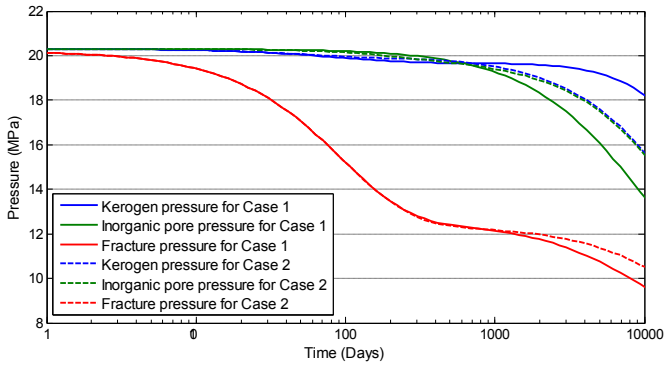

Fig. 12. Pressure evolution for Case 1: $D_{k0} = 1.0 \times 10^{-20}$ m^2/s; Case 2: $D_{k0} = 1 \times 10^{-18}$ m^2/s (fitted from Figs. 8 and 10).

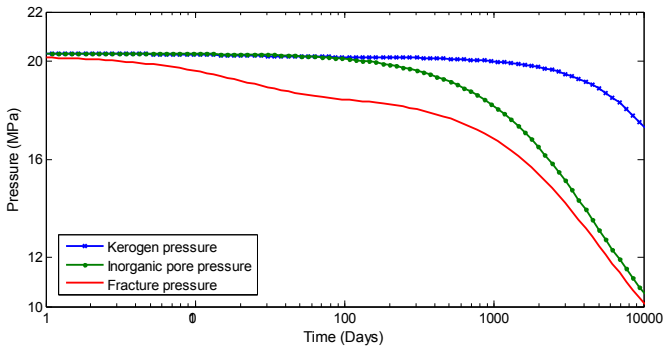

Fig. 13. Pressure evolutions for the case of $k_{20} = 1.5 \times 10^{-2}$ md, $D_{k0} = 1 \times 10^{-20}$ m^2/s and $k_{f0} = 3.25 \times 10^{-17}$ m^2.

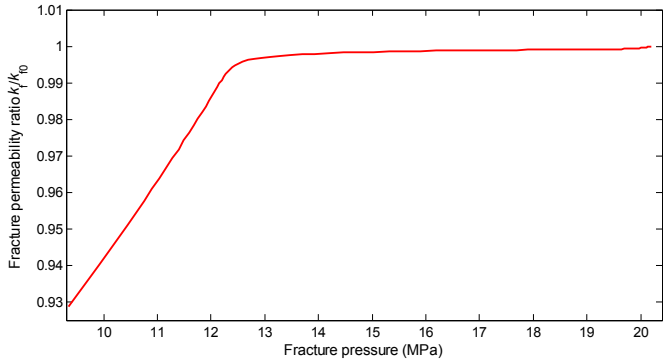

Fig. 14. Evolution of fracture permeability ratio together with fracture pressure.

gradient between fracture system and inorganic system drives the free gas in the inorganic matrix to flow to the fracture network, resulting in pore pressure drawdown. Since the rate of diffusion is relatively slow compared to flow within the inorganic matrix and fracture, the drop of pressure in the kerogen lags. This shows that the flow processes are sequential – desorbed gas may only flow following drawdown in the inorganic matrix-fracture components. This result is consistent with previous studies (Kang et al., 2011; Akkutlu et al., 2012) shown in Fig. 9. During gas depletion, a portion of the shale gas desorbs and transports first inside kerogen matrix system, and then into the inorganic matrix system, ultimately flowing towards the fracture system and reaching the production well.

Fig. 10 shows pressure evolution for the case where the diffusion coefficient of CH_4 in kerogen is 1.0×10^{-18} m^2/s. Due to the larger diffusion coefficient (two orders of magnitude larger than that for the former case), pressures in the kerogen and the inorganic pores evolve in unison and decline slower than the fracture pressure. The two systems reach a state of dynamic equilibrium with the same gas concentration due to the same gas pressure. In this state the net mass exchange rate of free gas flow from the inorganic matrix to the fracture network is approximately double that of free gas diffusion from the kerogen matrix to the inorganic matrix. Mechanistically, the net quantity of gas flow to the fracture system is drawn from both kerogen and inorganic matrix, concurrently and in equal quantity under this dynamic equilibrium. In this sense, even though the gas flow governing equations (Eqs. (34) and (43)) represent flow in series, the flow is virtually a special case of 'parallel flow,' as shown in Fig. 11.

The evolution of pressure for the two cases of $D_{k0} = 1.0 \times 10^{-20}$ m^2/s (Fig. 8) and $D_{k0} = 1.0 \times 10^{-18}$ m^2/s (Fig. 10) is fitted in Fig. 12. Pressure is drawdown only after 1000 d. Due to the enhancement of the diffusion coefficient, the pressure in the kerogen declines faster after 1000 d, while the pressure in the inorganic matrix and the fracture system decline more slowly after 1000 d. This phenomena indicates that during the depletion stage 1 d–1000 d, free gas in the fracture network and inorganic matrix dominate the response, and the enhancement of diffusion coefficient in kerogen has little effect on pressure evolution and gas depletion during this period. After the depletion of 1000 d, a significant portion of desorbed gas in the kerogen begins to contribute, and the enhancement of the diffusion coefficient of gas in kerogen will then supply the inorganic matrix and fracture system faster, leaving these two systems at a relatively higher pressure to keep the pressure difference between the fracture and well. This process enhances gas production rate at the later stage. This also supports the phenomena in Fig. 7 that the simulation result deviates from field data at later time. The effect of diffusion coefficient on production will be discussed further in Section 4.4.3.

Fig. 13 presents the evolution of gas pressure in the kerogen, inorganic matrix and fracture where the intrinsic permeability of the inorganic matrix is 1.5×10^{-2} md, close to intrinsic permeability of the fracture (3.25×10^{-17} m^2). The inorganic pore pressure declines much faster than that in the kerogen and almost catches up with the rate of decline in the fracture pressure. This result is consistent with previous observations (Peng et al., 2015), in which gas flow into the hydraulic fracture comes from both the inorganic pores and the natural fracture network. The gas flow also follows a sequential pattern.

From Figs. 8, 10 and 13, the diffusion coefficient of CH_4 in the kerogen matrix and the inorganic matrix permeability are two

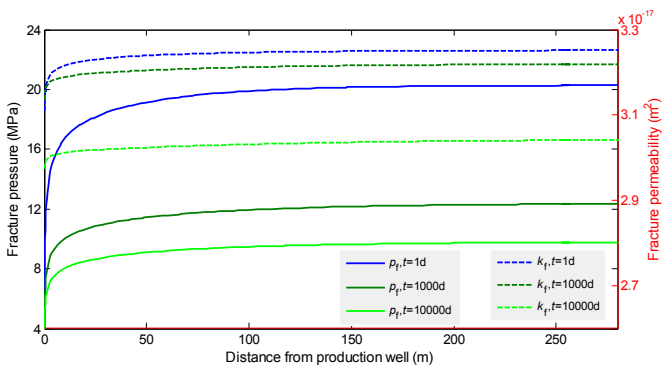

Fig. 15. Fracture pressure and permeability distribution along a diagonal x = y, x ∈ [0.071 m, 200 m](t = 1 d, 1000 d, 10,000 d).

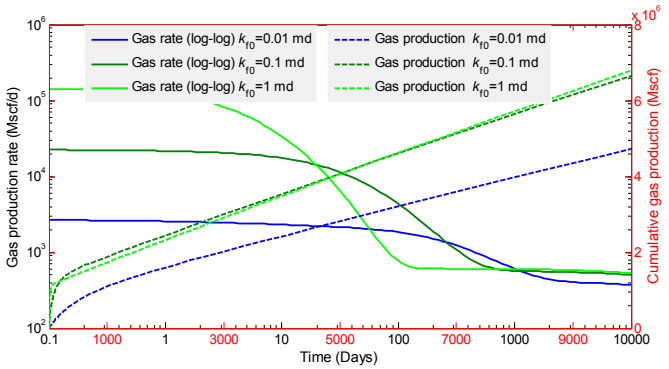

Fig. 16. Effect of fracture intrinsic permeability on log-lot plot of gas production rate vs. time and cumulative gas production in the normal time space.

important factors that influence pressure evolution in the kerogen and the inorganic matrix, and therefore influence the gas depletion process. The higher diffusion coefficient and inorganic matrix permeability could effectively enhance gas production rate and cumulative gas production. This topic will be discussed in a later section.

4.2. Permeability evolution

Fracture permeability decreases with a decrease in fracture pressure shown in Fig. 14. The dynamic permeability of a fractured porous system is controlled by sorption-induced swelling (Seidle et al., 1995; Wang et al., 2012b) and poromechanical dilation (Somerton et al., 1975; Durucan and Edwards, 1986; Jasinge et al., 2011). The skeletal stresses in the fracture system increase as gas pressure decreases, causing the contraction of the fracture system, while there is no desortive effect in the fracture system. The reduction of fracture permeability coincides with fracture contraction. From Fig. 14, it is also observed that k_f changes very little before the fracture pressure declines to 13 MPa while it declines sharply with the further decrease of p_f. This might result from that at the early stage of gas depletion, pore pressures in the fracture system declines much slower than that at the later stage, so the contractional strain of the fracture is relatively small and the reduction in permeability of the fracture is small.

4.3. Distribution of fracture pressure and permeability

Boundary effects can influence the pressure and permeability distribution within the reservoir as shown on a diagonal section through the well (Fig. 15). Fig. 15 illustrates that fracture pressure near the production well is closer to the well pressure p_w, where gas depletion is earlier and faster. The evolution of fracture permeability close to the well also occurs first. From the figure, pressures and permeability at a distance greater than ~50 m from the production well retains a uniform distribution.

4.4. Sensitivity analysis of effects on gas production rate and cumulative gas production

A useful facility of modeling is the ability to examine the sensitivity of the production rate to reservoir properties – which may be valuable for production well design and management. In this work, a sensitivity analysis of parameters affecting shale gas production rate and cumulative gas production is completed. This includes the respective roles of the intrinsic permeability of the fractures, the intrinsic permeability of the inorganic matrix, the diffusion coefficient of CH_4 in kerogen together with total organic content (TOC), the fracture spacing and the fracture intrinsic porosity.

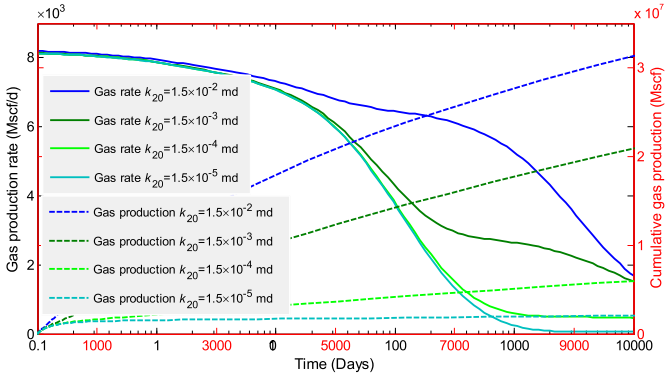

Fig. 17. Effect of intrinsic permeability of the inorganic matrix on gas production rate and cumulative gas production.

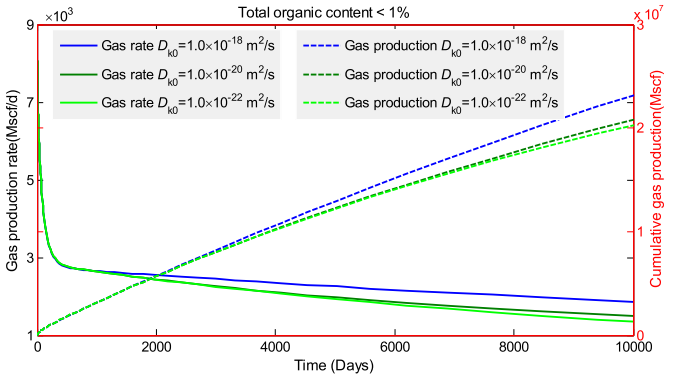

Fig. 18. Effect of diffusion coefficient of CH_4 in kerogen on gas production rate and cumulative gas production for the case of TOC < 1%.

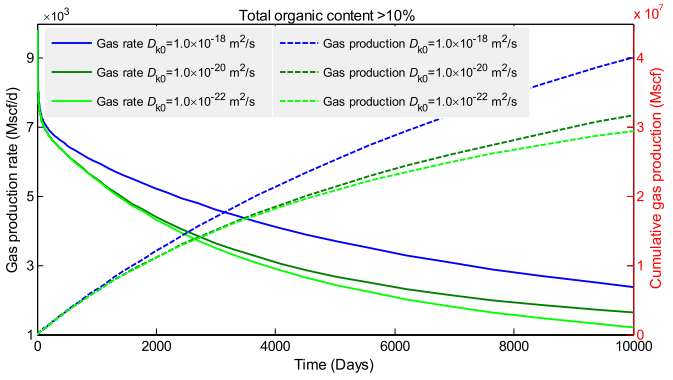

Fig. 19. Effect of diffusion coefficient of CH_4 in kerogen on gas production rate and cumulative gas production for the case of TOC > 10%.

4.4.1. Effect of fracture intrinsic permeability

As shown in Fig. 16, the contribution of fracture intrinsic permeability can be significant in shale plays. It is apparent that the reservoir with the higher fracture intrinsic permeability has a higher gas production rate in the early stages (0.1 d–20 d), lower gas production rate mid-stage and reinvigorated higher gas production rate again at late-stage (1000 d–10,000 d), relative to production rates for a reservoir with a permeability two orders of

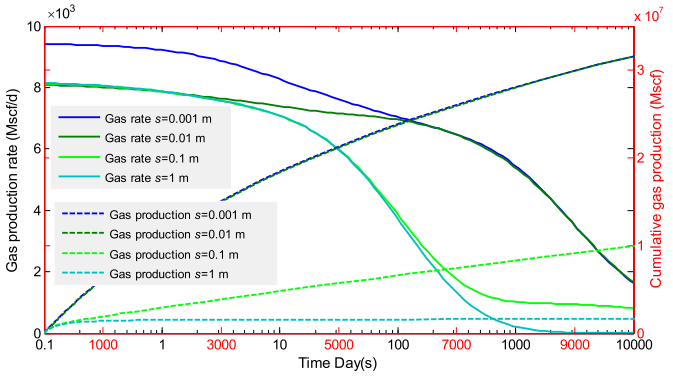

Fig. 20. Effect of fracture spacing on gas production rate and cumulative gas.

magnitude lower. At early time (0.1 d–20 d), gas production rate is approximately proportional to the intrinsic permeability of the fracture, because the free gas flow within the fracture network (obeying Darcy's law) dominates at this stage. In the mid-stage, as the free gas in the fracture network is depleted, fracture pressure drops more quickly due to higher fracture permeability. The production rate for the case with lower intrinsic permeability of the fracture system slowly overtakes that for the higher fracture intrinsic permeability – this is due to the greater fracture pressure gradient at mid-stage. At late-stage (1000 d–10,000 d), the production rate is relatively low but remains stable in the long term due to continuous desorption from the kerogen. The reservoir with the higher fracture intrinsic permeability has a higher production rate than the low permeability reservoir, again at this stage. This is because the reservoir with a higher permeability fracture network provides a more permeable channel for gas to flow to the production well. This study confirms that fracture treatment is an effective way to increase the permeability of the fracture network, thus enhancing shale gas production.

Also apparent from Fig. 16 is that cumulative gas production increases with an increase of k_{f0} from 0.01 md to 0.1 md, while it increases only slightly with an increase of k_{f0} from 0.1 md to 1 md. The gas production rate has the same trend at late-time (1000 d–10,000 d). This is because the permeability of the inorganic matrix and the diffusion coefficient of CH_4 in kerogen are the main rate-limiting factor – discussed in the next sections. Any further increase in fracture permeability, therefore, would not necessarily enhance gas production.

4.4.2. Effect of the intrinsic permeability of the inorganic matrix

The role that the intrinsic permeability of the inorganic matrix plays in gas production is explored in this section. As is shown in Fig. 17, at early-time, the increment of production rate due an increase in the intrinsic permeability of the inorganic matrix is negligible. This is because the gas flow within the inorganic matrix is secondary compared to gas flow within the fracture network (at this stage). At late-stage, however, the production rate and cumulative gas production are remarkably influenced by the permeability of the inorganic matrix. The reservoir with the higher intrinsic permeability of the inorganic matrix has simultaneously the higher gas production rate and greater cumulative gas production at this stage. Therefore, the permeability of the inorganic matrix is one of the main factors limiting gas production at later stages. In this sense, some methods of mechanical or chemical stimuli could enhance the matrix permeability as an effective way to enhance gas production rate and cumulative gas production at later stage, thus notably enhancing cumulative gas production.

4.4.3. Effect of diffusion coefficient of CH_4 in kerogen together with TOC

Organic carbon in the form of kerogen is the remnants of ancient life preserved in shale reservoirs. By definition, total organic content (TOC) is proportional to the weight fraction of kerogen in the shale reservoir as

$$TOC = K_{TOC} \times \left(\frac{\rho_{ker}}{\rho_{shale}}\right) \times \frac{a^3}{(a+c)^3} \tag{48}$$

where ρ_{ker} is the density of kerogen and ρ_{shale} is the density of the shale reservoir. a and c are kerogen matrix width and inorganic matrix width within the REV, respectively. K_{TOC} is a kerogen correction factor (Crain, 2000) that ranges from 0.68 to 0.90, depending on the maturity of the kerogen. The default value of K_{TOC} is 0.80. That is, that carbon accounts for ~80% (by weight) in a typical kerogen.

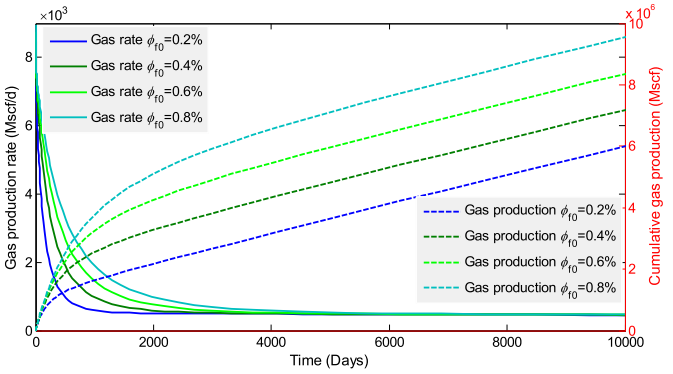

Fig. 21. Effect of fracture intrinsic porosity on gas production rate and cumulative gas production.

Gas diffusion within the kerogen contributes significantly to total gas production by continuously supplying gas from the kerogen surface to the pore spaces (Shabro et al., 2012; Moghanloo et al., 2013). As shown in Figs. 18 and 19, the effect of the diffusion coefficient of CH_4 in kerogen on gas production is non-negligible. For TOC < 1%, D_k has a relatively small impact on gas production rate and cumulative gas production; while for TOC > 10%, the contribution of D_k to production significant. These results are consistent with prior observations (Moghanloo et al., 2013; Etminan et al., 2014). Even though diffusion within kerogen nanopores is very slow due to extremely low diffusion rates conditioned by the diffusion coefficient, the diffusive gas flow could be dramatic due to extremely large surface area in kerogen. Therefore, the diffusion coefficient of CH_4 in the kerogen is a critical factor influencing gas production in shale reservoirs with higher TOC.

4.4.4. Effect of fracture spacing and fracture intrinsic porosity

As is shown in Fig. 20, gas production rate and cumulative gas production are sensitive to fracture spacing s. The overall trend is that gas production rate is higher for smaller fracture spacing, but gas rate shows little change at very early-time (<10 days) if $s > 0.01$ m and also little change at late-time (>100 days) if $s < 0.01$ m. Cumulative gas production increases with an increase in fracture spacing from 1×10^{-4} m to 1 m, but is negligible for spacing s increased from 0.01 to 0.1 m. Fig. 21 illustrates the impact of fracture intrinsic porosity on gas production rate and cumulative gas production. The increment of cumulative gas production with respect to time is near proportional to Φ_{f0}, which results from the shale reservoir with higher Φ_{f0} providing more potential flow paths during gas production. This study suggests that fracture treatment that reduces fracture spacing and enhances fracture porosity would be useful to enhance total gas production.

5. Conclusions

A multi-scale gas transport model, including molecular diffusion and viscous flow, and a general triple porosity model considering kerogen, inorganic matrix rock and a fracture system, is developed to represent hydrocarbon recovery from shale. The model is verified against field data of gas production rate. The model couples gas flow within the kerogen, inorganic matrix and fracture system with the deformation of shale, based on the principle of effective stress applied to triple-porosity media. The porosity and permeability model is based on the theory of poroelasticity, and as such is applicable to the full range of mechanical boundary conditions,

from invariant total stress to restrained displacement. Using the proposed triple porosity model, evolution of pressure and permeability in triple media is analyzed and some important factors affecting shale gas production explored. The main observations and conclusions are summarized below.

The pattern of gas flow is sequential during gas depletion. Fracture pressure first declines, followed by a decline in the inorganic phase and then in the kerogen. The evolution of pressure is closely related with the intrinsic gas diffusion coefficient in the kerogen and the intrinsic permeabilities of the inorganic matrix and fracture – and these in turn are also controlled by the evolution of pore pressures.

The contribution of the intrinsic permeability of the fracture to gas production is significant since it is the dominant permeable channel in the shale reservoir. Appropriate fracturing treatments can enhance fracture permeability, thus enhancing total shale gas production. This is true only to a certain level, as beyond a point, further fracturing treatment cannot efficiently enhance shale gas production due to the intrinsic low matrix permeability and extremely low gas diffusion coefficient in the kerogen.

The permeability of the inorganic matrix and the gas diffusion coefficient in the kerogen are the two key rate-limiting factors that potentially guarantee long-term gas production with an improved rate. The inorganic matrix provides a large area of permeable channels for flow, while kerogen provides a large amount of adsorbed gas and dramatic diffusive gas flow due to extremely large surface area of the kerogen. Shale reservoirs with higher inorganic matrix permeability and gas diffusion coefficient in the kerogen can notably enhance gas production. The effect of gas diffusion coefficient in the kerogen on gas production is more apparent for shale reservoirs with higher total organic content. The fracture intrinsic porosity has a positive correlation to gas production, while fracture spacing has a negative correlation to gas production.

Acknowledgement

This work was supported by the State Key Development Program for Basic Research of China (Grant No. 2013CB227900), the State Key Development Program for Basic Research of China (Grant No. 2015CB251601). The financial support provided by China Scholarship Council (CSC) is also gratefully acknowledged.

Appendix

Assuming that the total volume V of the porous inorganic matrix system is divided into two parts: a pore system containing the interconnected pore space of volume V_p, and the combined volume of the solid phase and isolated pores V_s; $V = V_p + V_s$. The porosity of the inorganic matrix system is defined as the ratio of V_p to V, $\Phi_2 = V_p/V$. According to Eq. (10), the relations are

$$\begin{cases} \varepsilon_{v2} = \dfrac{\Delta V}{V} = \dfrac{1}{K_2}\left[\overline{\sigma} - \left(\gamma p_f + \beta p_2\right)\right] \\ \varepsilon_{vp2} = \dfrac{\Delta V_p}{V_p} = \dfrac{1}{K_{p2}}\left[\overline{\sigma} - \left(\gamma_1 p_f + \beta_1 p_2\right)\right] \end{cases} \tag{49}$$

There is no gas sorption effect in inorganic matrix system, and the volumetric variation of the porous medium satisfies the Betti-Maxwell reciprocal theorem, $(\partial V/\partial p_2)_{\overline{\sigma}} + (\partial V/\partial p_f)_{\overline{\sigma}} = -(\partial V_p/\partial \overline{\sigma})_{p_2,p_f}$, i.e., the total volume increment of the porous inorganic matrix system ΔV caused by the application of pore pressures p_2 and p_f is the same as the volume reduction of the pore ΔV_p due to the application of the mean compressive stress $\overline{\sigma}$ (Detournay and Cheng, 1993).

K_{p2} is the bulk modulus for the pore volumetric strain. According to the Betti-Maxwell reciprocal theorem, we obtain

$$K_{p2} = \frac{\Phi_2}{\beta + \gamma} K_2 \tag{50}$$

β, β_1, γ and γ_1 are dimensionless effective stress coefficients, defined as

$$\begin{cases} \beta = 1 - \dfrac{K_2}{K_{s2}} \\ \beta_1 = 1 - \dfrac{K_{p2}}{K_{s2}} \\ \gamma = 1 - \dfrac{K_f}{K_{sf}} \\ \gamma_1 = 1 - \dfrac{K_{pf}}{K_{sf}} \end{cases} \tag{51}$$

where K_2 is the bulk modulus of the porous inorganic system, K_{s2} is bulk modulus of the inorganic grains. Due to the fractal characteristics of the porous medium, we assume that the ratio of the bulk modulus of the triple fractured porous shale K to the bulk modulus of the porous inorganic system K_2 and the ratio of K_2 to K_{s2} are of equal magnitude ($K/K_2 = K_2/K_{s2}$). Similarly, K/K_f is the same as K_f/K_{sf}. i.e., the effective stress coefficient β is shared by both the inorganic system and the whole fractured porous system, and the effective stress coefficient γ is shared by both fracture system and the whole fractured porous system.

The change in porosity is defined as

$$d\Phi_2 = d(V_P/V) = \frac{V_P}{V}\left(\frac{dV_P}{V_p} - \frac{dV}{V}\right) = \Phi\left(\frac{dV_P}{V_p} - \frac{dV}{V}\right) \tag{52}$$

If the change in porosity of inorganic system is small, we obtain

$$\Delta\Phi_2 = \Phi_2\left(\frac{\Delta V_P}{V_p} - \frac{\Delta V}{V}\right) \tag{53}$$

Due to the fractal characteristics of the porous medium, we assume that $K_{pf}/K_f = K_{p2}/K_2$. Combining (49) and (51) yields

$$\begin{aligned} \Delta\Phi_2 &= \Phi_2\left(\frac{1}{K_{p2}} - \frac{1}{K_2}\right)\left(\overline{\sigma} - p_2 - p_f\right) \\ &= \frac{1}{K_2}(\beta + \gamma - \Phi_2)\left(\overline{\sigma} - p_2 - p_f\right) \end{aligned} \tag{54}$$

Considering that the initial volumetric stain is zero, integrating Eq. (54) yields the final porosity model

$$\Phi_2 = \frac{1}{1 + S_2}\left[(1 + S_{20})\Phi_{20} + (\beta + \gamma)(S_2 - S_{20})\right] \tag{55}$$

$$S_2 = \frac{1}{K_2}\left(\overline{\sigma} - p_2 - p_f\right) \tag{56}$$

Combining Eq. (55) with (56), we obtain S_2, S_{20} and other parameters as shown in Section 2.3.1.

Nomenclature

σ_{ij}	Component of the total stress tensor [Pa]
f_i	Component of the body force [Pa m^{-1}]
σ_{ij}'	Component of the effective stress for the fractured porous shale [Pa]
δ_{ij}	The Kronecker delta

p	Pressure [Pa]
α, β, γ	The effective stress coefficients for kerogen, inorganic matrix and fracture system
K	Bulk modulus [MPa]
E	Young's modulus [MPa]
G	Shear modulus [MPa]
ν	Poisson's ratio
λ	Lame constant [MPa]
u	Displacement [m]
ε_s	Sorption-induced strain
ε_L	Langmuir volumetric strain
P_L	Langmuir pressure [Pa]
V_L	Langmuir volume [m^3 kg^{-1}]
σ^e_{ij}	Component of the effective stress tensor in each system [Pa]
ε_{ij}	Component of the strain tensor
$\overline{\sigma}$	Mean compressive stress [Pa]
ε_v	Volumetric strain
ε_l	Total linear strain
a, c	Width of the kerogen block and inorganic block, respectively [m]
b	Equivalent fracture aperture [m]
s	Fracture spacing (a+c) [m]
N_1	Parameter defined by the elastic properties and the size of REV [m MPa^{-1}]
N_2, N_3	Parameters defined by the elastic properties and the size of REV [MPa^{-1}]
Φ	Porosity
k	Permeability [m^2]
m	Gas mass content [kg m^{-3}]
D	Molecular diffusion coefficient [m^2 s^{-1}]
D_k	Modified diffusion coefficient of CH4 in kerogen [m^2 s^{-1}]
τ	Tortuosity of the kerogen matrix
Q_{1-2}, Q_{2-f}	Gas exchange rate [kg m^{-3} s^{-1}]
Q_s	Mass source due to external injection or extraction [kg m^{-3} s^{-1}]
ρ_g, ρ, ρ_{ker}	Gas density, density of shale, density of kerogen [kg m^{-3}]
Mg	Gas molecular weight [kg mol^{-1}]
ρ_{ga}	Gas density at standard condition [kg m^{-3}]
τ'	Diffusive time [s]
σ_1,σ_2	Shape factor [m^{-2}]
q_g	Darcy velocity vector [m s^{-1}]
μ	Gas viscosity [Pa s]
ω_1	Transfer coefficient between the kerogen matrix and the inorganic matrix [s^{-1}]
ω_2	Transfer coefficient between the inorganic matrix and fracture [s^{-1}]
F_y, F_x	Overburden stress, horizontal crustal stress [Pa]
γ'	Overburden stress gradient [Pa m^{-1}]
h	Depth of shale reservoir [m]
λ'	Lateral stress ratio
p_w	Well pressure [Pa]
L	Horizontal well length [m]
p_{init}	Initial reservoir pressure [Pa]
T	Reservoir temperature [K]
R	Universal gas constant [J K^{-1} mol^{-1}]
TOC	Total organic content
K_{TOC}	Kerogen correction factor
V	Total volume [m^3]
V_p	Volume of pore space [m^3]
V_s	Combined volume of the solid phase and isolated pores [m^3]
Δ	Increment of a variable
K_p	Bulk modulus for the pore volumetric strain [MPa]
K_s	Bulk modulus of grains [MPa]

Subscripts

i,j and *k*	Indices running from 1 to 3
0	Initial value of the variable
1	Kerogen system
2	Inorganic matrix
f	Fracture system

References

Aadnoy, B., Looyeh, R., 2011. Petroleum Rock Mechanics: Drilling Operations and Well Design. Gulf Professional Publishing.

Akkutlu, I.Y., Fathi, E., others, 2012. Multiscale gas transport in shales with local kerogen heterogeneities. SPE J. 17, 1–002.

Al Ahmadi, H.A., Almarzooq, A.M., Wattenbarger, R.A., others, 2010. Application of linear flow analysis to shale gas wells-field cases. In: SPE Unconventional Gas Conference. Society of Petroleum Engineers.

Al-Ahmadi, H.A., Wattenbarger, R.A., others, 2011. Triple-porosity models: one further step towards capturing fractured reservoirs heterogeneity. In: SPE/DGS Saudi Arabia Section Technical Symposium and Exhibition. Society of Petroleum Engineers.

Ambrose, R.J., Hartman, R.C., Diaz-Campos, M., Akkutlu, I.Y., Sondergeld, C.H., others, 2012. Shale gas-in-place calculations part I: new pore-scale considerations. SPE J. 17, 219–229.

Bello, R.O., Wattenbarger, R.A., others, 2010. Modelling and analysis of shale gas production with a skin effect. J. Can. Pet. Technol. 49, 37–48.

Chilingar, G.V., 1964. Relationship between porosity, permeability, and grain-size distribution of sands and sandstones. Dev. Sedimentol. 1, 71–75.

Crain, E., 2000. Crain's Petrophysical Handbook. Spectrum.

Dehghanpour, H., Shirdel, M., others, 2011. A triple porosity model for shale gas reservoirs. In: Canadian Unconventional Resources Conference. Society of Petroleum Engineers.

Detournay, E., Cheng, A.H.D., 1993. Fundamentals of poroelasticity. In: Anal. Des. Methods Compr. Rock Eng. Princ. Pract. Proj., pp. 113–171.

Durucan, S., Edwards, J., 1986. The effects of stress and fracturing on permeability of coal. Min. Sci. Technol. 3, 205–216.

Elsworth, D., Bai, M., 1992. Flow-deformation response of dual-porosity media. J. Geotech. Eng. 118, 107–124.

Etminan, S.R., Javadpour, F., Maini, B.B., Chen, Z., 2014. Measurement of gas storage processes in shale and of the molecular diffusion coefficient in kerogen. Int. J. Coal Geol. 123, 10–19.

Goodway, B., Varsek, J., Abaco, C., 2006. Practical Applications of P-wave AVO for Unconventional Gas Resource Plays, pp. 52–65. Part 2.

Huang, T., Guo, X., Chen, F., 2015. Modeling transient flow behavior of a multiscale triple porosity model for shale gas reservoirs. J. Nat. Gas Sci. Eng. 23, 33–46.

Jasinge, D., Ranjith, P., Choi, S.-K., 2011. Effects of effective stress changes on permeability of latrobe valley brown coal. Fuel 90, 1292–1300.

Javadpour, F., Fisher, D., Unsworth, M., others, 2007. Nanoscale gas flow in shale gas sediments. J. Can. Pet. Technol. 46, 55–61.

Javadpour, F., 2009. Nanopores and apparent permeability of gas flow in mudrocks (shales and siltstone). J. Can. Pet. Technol. 48, 16–21.

Kang, S.M., Fathi, E., Ambrose, R.J., Akkutlu, I.Y., Sigal, R.F., others, 2011. Carbon dioxide storage capacity of organic-rich shales. SPE J. 16, 842–855.

Katsube, T., 2000. Shale permeability and pore-structure evolution characteristics. Geol. Surv. Can. Rep. E15.

Langmuir, I., 1918. The adsorption of gases on plane surfaces of glass, mica and platinum. J. Am. Chem. Soc. 40, 1361–1403.

Li, X., Elsworth, D., 2014. Geomechanics of CO2 enhanced shale gas recovery. J. Nat. Gas Sci. Eng. 26, 1607–1619.

Lim, K., Aziz, K., 1995. Matrix-fracture transfer shape factors for dual-porosity simulators. J. Pet. Sci. Eng. 13, 169–178.

Liu, J., Elsworth, D., et al., 1999. Linking stress-dependent effective porosity and hydraulic conductivity fields to RMR. Int. J. Rock Mech. Min. Sci. 36, 581–596.

Liu, Q., Cheng, Y., Zhou, H., Guo, P., An, F., Chen, H., 2015. A mathematical model of coupled gas flow and coal deformation with gas diffusion and klinkenberg effects. Rock Mech. Rock Eng. 48, 1163–1180.

Loucks, R.G., Reed, R.M., Ruppel, S.C., Jarvie, D.M., 2009. Morphology, genesis, and distribution of nanometer-scale pores in siliceous mudstones of the Mississippian Barnett Shale. J. Sediment. Res. 79, 848–861.

Mengal, S.A., 2010. Accounting for Adsorbed Gas and Its Effect on Production Behavior of Shale Gas Reservoirs. Texas A&M University.

Mian, C., Zhida, C., et al., 1999. Effective stress laws for multi-porosity media. Appl. Math. Mech. 20, 1207–1213.

Moghanloo, R., Davudov, D., Javadpour, F., 2013. Contribution of methane molecular diffusion in kerogen to gas-in-place and production. In: SPE Western Regional & AAPG Pacific Section Meeting, Monterey, CA, USA.

Mora, C., Wattenbarger, R., others, 2009. Analysis and verification of dual porosity and CBM shape factors. J. Can. Pet. Technol. 48, 17–21.

Palmer, I., Mansoori, J., others, 1996. How permeability depends on stress and pore pressure in coalbeds: a new model. In: SPE Annual Technical Conference and Exhibition. Society of Petroleum Engineers.

Peng, Y., Liu, J., Pan, Z., Connell, L.D., 2015. A sequential model of shale gas transport under the influence of fully coupled multiple processes. J. Nat. Gas Sci. Eng. 27,

808–821.
Robertson, E., Christiansen, R., et al., 2006. A Permeability Model for Coal and Other Fractured, Sorptive-elastic Media. Idaho National Laboratory. INL/EXT-06-11830.
Seidle, J.R., Huitt, L., others, 1995. Experimental measurement of coal matrix shrinkage due to gas desorption and implications for cleat permeability increases. In: International Meeting on Petroleum Engineering. Society of Petroleum Engineers.
Shabro, V., Torres-Verdin, C., Sepehrnoori, K., others, 2012. Forecasting gas production in organic shale with the combined numerical simulation of gas diffusion in kerogen, Langmuir desorption from kerogen surfaces, and advection in nanopores. In: SPE Annual Technical Conference and Exhibition. Society of Petroleum Engineers.
Shi, J., Durucan, S., 2004. Drawdown induced changes in permeability of coalbeds: a new interpretation of the reservoir response to primary recovery. Transp. Porous Media 56, 1–16.
Somerton, W.H., Söylemezoglu, I., Dudley, R., 1975. Effect of stress on permeability of coal. In: International Journal of Rock Mechanics and Mining Sciences & Geomechanics Abstracts. Elsevier, pp. 129–145.
Song, B., 2010. Pressure Transient Analysis and Production Analysis for New Albany Shale Gas Wells. Texas A&M University.
Tivayanonda, V., Apiwathanasorn, S., Economides, C., Wattenbarger, R., others, 2012. Alternative interpretations of shale gas/oil rate behavior using a triple porosity model. In: SPE Annual Technical Conference and Exhibition. Society of Petroleum Engineers.
Wang, J., Kabir, A., Liu, J., Chen, Z., 2012a. Effects of non-Darcy flow on the performance of coal seam gas wells. Int. J. Coal Geol. 93, 62–74.
Wang, S., Elsworth, D., Liu, J., 2012b. A mechanistic model for permeability evolution in fractured sorbing media. J. Geophys. Res. Solid Earth 117.
Wang, J., Liu, J., Kabir, A., 2013. Combined effects of directional compaction, non-Darcy flow and anisotropic swelling on coal seam gas extraction. Int. J. Coal Geol. 109, 1–14.
Warren, J., Root, P.J., others, 1963. The behavior of naturally fractured reservoirs. Soc. Pet. Eng. J. 3, 245–255.
Wasaki, A., Akkutlu, I.Y., others, 2014. Permeability of organic-rich shale. In: SPE Annual Technical Conference and Exhibition. Society of Petroleum Engineers.
Wattenbarger, R.A., El-Banbi, A.H., Villegas, M.E., Maggard, J.B., others, 1998. Production analysis of linear flow into fractured tight gas wells. In: SPE Rocky Mountain Regional/low-permeability Reservoirs Symposium. Society of Petroleum Engineers.
Wu, Y., Liu, J., Elsworth, D., Chen, Z., Connell, L., Pan, Z., 2010. Dual poroelastic response of a coal seam to CO2 injection. Int. J. Greenh. Gas Control 4, 668–678.
Wu, Y., Liu, J., Elsworth, D., Siriwardane, H., Miao, X., 2011. Evolution of coal permeability: contribution of heterogeneous swelling processes. Int. J. Coal Geol. 88, 152–162.
Yan, B., Wang, Y., Killough, J.E., 2013a. Beyond dual-porosity modeling for the simulation of complex flow mechanisms in shale reservoirs. Comput. Geosci. 1–23.
Yan, F., Han, D., others, 2013b. Measurement of elastic properties of kerogen. In: 2013 SEG Annual Meeting. Society of Exploration Geophysicists.
Zhang, H., Liu, J., Elsworth, D., 2008. How sorption-induced matrix deformation affects gas flow in coal seams: a new FE model. Int. J. Rock Mech. Min. Sci. 45, 1226–1236.
Zhang, M., Yao, J., Sun, H., Zhao, J., Fan, D., Huang, Z., Wang, Y., 2015. Triple-continuum modeling of shale gas reservoirs considering the effect of kerogen. J. Nat. Gas Sci. Eng. 24, 252–263.
Ziarani, A.S., Aguilera, R., 2012. Knudsen's permeability correction for tight porous media. Transp. Porous Media 91, 239–260.